AN OVER-AND-OUT HALO CORONAL MASS EJECTION DRIVEN BY THE FULL ERUPTION OF A KINKED FILAMENT

Jiayan Yang[1,2], Yunchun Jiang[1], Yi Bi[1], Haidong Li[1], Junchao Hong[1,3], Dan Yang[1,3], Ruisheng Zheng[1,3], and Bo Yang[1,3]

[1] National Astronomical Observatories/Yunnan Astronomical Observatory, Chinese Academy of Sciences, P.O. Box 110, Kunming 650011, China; yjy@ynao.ac.cn
[2] Key Laboratory for the Structure and Evolution of Celestial Objects, Chinese Academy of Sciences, Kunming 650011, China
[3] Graduate School of Chinese Academy of Sciences, Beijing 100049, China

ABSTRACT

Over-and-out coronal mass ejections (CMEs) represent a broad class of CMEs that come from flare-producing magnetic explosions of various sizes but are laterally far offset from the flare, and their productions can be depicted by the magnetic-arch-blowout scenario. In this paper, we present observations of an over-and-out halo CME from the full eruption of a small kinking filament in an emerging active region (AR). In combination with the results of a derived coronal magnetic configuration, our observations showed that the CME was associated with a coronal helmet streamer, and the filament was located in the northern outskirts of the streamer base. Formed along a neutral line where flux cancellation was forced by the emerging AR with the surrounding opposite-polarity magnetic field, the filament underwent a full, non-radial eruption along the northern leg of the streamer arcade, accompanied by a clockwise deflection of the eruption direction. As a characteristic property of kink instability, the eruption displayed a clear inverse γ shape, indicative of a writhing motion of the filament apex. Coronal dimmings, including a remote one, formed in opposite-polarity footprint regions of the streamer arcade during the eruption, and the consequent CME was laterally offset from the AR. These observations suggest that the kink instability is likely to be the driver in the eruption. The event can be well explained by putting this driver into the magnetic-arch-blowout model, in which the eruption-direction deflection and the full-eruption nature of the kinking filament are caused by the guiding action of the streamer arcade and the external reconnection between them.

Key words: Sun: activity – Sun: coronal mass ejections (CMEs) – Sun: filaments, prominences – Sun: flares – Sun: magnetic topology

1. INTRODUCTION

The background magnetic fields play an important role in the early dynamic behavior of coronal mass ejection (CME). For example, the ambient magnetic field structure can impose additional action on determining the speed of the halo CMEs (Liu 2007), while the deflection or rotation of CMEs is mainly controlled by the magnetic field topology in the low corona (Cremades & Bothmer 2004; Lynch et al. 2009; Byrne et al. 2010; Gui et al. 2011; Shen et al. 2011; Sterling et al. 2011; Wang et al. 2011; Zuccarello et al. 2012). Consistent with previous results (Harrison 1986; Gopalswamy & Thompson 2000; Filippov & Gopalswamy 2001), Moore & Sterling (2007) recently concluded that, as a broad class of CMEs, the so-called over-and-out CMEs come from flare-producing magnetic explosions of various sizes but are laterally far offset from the flare. As first identified by Bemporad et al. (2005), an over-and-out CME can obviously originate from a flare in an outer flank of the base of a streamer. Moore & Sterling (2007) further proposed that all over-and-out CMEs are produced in basically the same way as depicted by the so-called magnetic-arch-blowout scenario: the magnetic explosion that produces the flare also produces a plasmoid that explodes up the leg of an outer loop of the arcade base of the streamer, blows out the top of this loop, and becomes the core of the CME. In particular, they gave an example to show that the production of a remote coronal dimming (Thompson et al. 1998) during an over-and-out CME provides the key clue to nicely confirm this scenario. More recently, Yang et al. (2011) also showed an over-and-out partial halo CME in association with the formation of a remote dimming. Under this scenario, it is clear that the

deflection of a CME from the eruptive source region is a natural result. The CMEs studied by Moore & Sterling (2007) and Yang et al. (2011) did not involve any filament eruption; thus, the initial growth of the CMEs cannot be traced. Jiang et al. (2009) showed that a non-radial filament eruption from the outer flank of a streamer base was guided by the streamer arcade in the inner corona and thus led to a radial over-and-out CME in the outer corona, but their event had no clear coronal dimming. Therefore, simultaneous observations of both early propagation and associated remote dimming in over-and-out CME events are of great help in understanding the magnetic-arch-blowout scenario and the deflection of CMEs.

The triggering and early growth of solar eruptive phenomena evidently result from either of two basically different mechanisms or from both acting in concert: (1) MHD instability or loss of equilibrium or/and (2) tether-cutting reconnection of the leg of the sheared core field (Moore & Sterling 2006). As an attractive triggering mechanism first suggested by Sakurai (1976), the MHD helical kink instability of the coronal flux rope recently received considerable attention (Fan 2005; Kliem et al. 2010). Because a rising kink-unstable flux rope is expected to undergo a writhing motion of the apex about the direction of ascent and thus to develop a helical axis shape by the conversion of twist helicity into writhe helicity (Rust & LaBonte 2005), an eruptive filament that shows an inverse γ shape or a spine rotation has been taken as strong evidence of a kink instability in some events (Webb et al. 2000; Romano et al. 2003; Alexander et al. 2006; Zhou et al. 2006; Green et al. 2007; Liu et al. 2008; Cho et al. 2009; Liu & Alexander 2009; Muglach et al. 2009; Karlický & Kliem 2010; Srivastava et al. 2010; Bi et al. 2011; Kumar et al. 2011). However, the eventual outcome
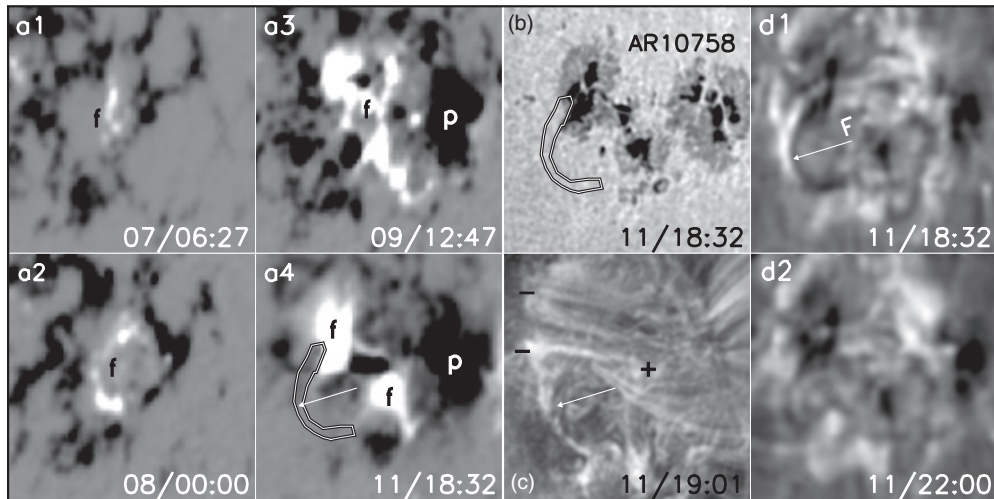
Figure 1. General evolution of the erupting region in MDI magnetograms (a1–a4) and in *TRACE* white-light (b), 171 Å (c), and BBSO Hα (d1–d2) images. The preceding/following ends of AR 10758 are labeled as "p"/"f," and the plus/minus signs mark the corresponding photospheric positive/negative polarities. The outlines of the eruptive filament, "F," determined from the 18:32 UT Hα image are superimposed as contours, and its centroid is indicated by the white arrows. The FOV is $110'' \times 110''$.

of a kink instability, i.e., whether it can lead to a full (Williams et al. 2005), a partial (Liu et al. 2007), or a failed (Ji et al. 2003) eruption, strongly depends on the interaction between the flux rope and magnetic environment and depends on the property of the overlying magnetic field as well (Török & Kliem 2005; Gibson & Fan 2006, 2008; Fan & Gibson 2007; Gilbert et al. 2007; Liu 2008). Although no observations have been reported so far, it is expected that an over-and-out CME could be driven by a kink instability also. Obviously, detailed investigations of such an event can provide valuable insight into the role of the ambient magnetic field in a kink instability.

On 2005 May 11, a small active region (AR) filament in NOAA AR 10758 (S11°W51°) erupted non-radially from an outer flank of the base of a coronal helmet streamer. The eruption was followed by an M1.1 flare and an over-and-out full halo CME laterally far offset from the flare. A remote coronal dimming formed in another flank of the streamer base during the eruption. Especially, the erupting filament displayed a clear inverse γ shape and a deflection of the eruption direction. In the paper, we present observations of the event and a comparison with the potential-field source-surface (PFSS) modeled streamer belt. This enables us to detail the relationship among the kinking filament eruption, the streamer arcade, the remote dimming, and the CME under the magnetic-arch-blowout scenario.

2. OBSERVATIONS

The filament eruption was covered by the observations from the Big Bear Solar Observatory (BBSO), the Chromospheric Helium Imaging Photometer (CHIP) at the Mauna Loa Solar Observatory (MLSO; MacQueen et al. 1998), the *Transition Region and Coronal Explorer* (*TRACE*; Handy et al. 1999), the Extreme Ultraviolet Imaging Telescope (EIT; Delaboudinière et al. 1995) on board the *Solar and Heliospheric Observatory* (*SOHO*), and the Solar X-Ray Imager (SXI; Hill et al. 2005) on board the *GOES-12* satellite, respectively. The BBSO provides full-disk Hα images with a cadence of 1 minute and a pixel size of about $1''$. CHIP provides full-disk He I 10830 Å velocity images acquired at seven filter positions covering the spectral region from 10826 Å to 10834 Å, which give a measure of the line-of-sight velocity component over the range of $\pm 100 \, \mathrm{km \, s^{-1}}$

(Toma et al. 2005). *TRACE* provides white-light, 171 Å, and 1600 Å images for the event, with a varied cadence and a pixel size of $0''.5$. Unfortunately, there are some gaps in CHIP and *TRACE* data, and the limited filed of view (FOV) of *TRACE* only partially covered the eruption. Routinely, EIT continuously obtains full-disk 195 Å images with a 12-minute cadence and a pixel resolution of $2''.6$, while 171, 284, and 304 Å images are taken only once every 6 hr. From 16:41 to 19:32 UT on 2005 May 11, however, EIT observed the eruptive region on the Selected-Areas-Mode, and thus 195 Å images with a higher temporal resolution of about 1 minute were obtained for the eruption. SXI provides full-disk soft X-ray (SXR) images in the wavelength range of 6–60 Å (sensitive to temperatures of 10^6–10^7 K) with a resolution of $5''$ pixel^{-1}. On 2005 May 11, SXR images observed with the polyimide thin filter position were available at a cadence of 4 minutes.

To identify the associated CME, we used white-light observations from the Mark IV coronameter (MK4) at MLSO, the C2 and C3 data from the Large Angle and Spectrometric Coronagraphs (LASCO; Brueckner et al. 1995) on board *SOHO*, and the CME height–time data available at the LASCO Web site. The magnetic field configuration was also examined using 96-minute cadence full-disk magnetograms with a pixel size of $2''$ from the Michelson Doppler Imager (MDI; Scherrer et al. 1995) on board *SOHO*. Finally, we used SXR light curves observed by *GOES* to track the flare time.

3. RESULTS

As an emerging AR, the general evolution of AR 10758 is shown in Figure 1. Its following polarity, "f," first appeared at about 06:00 UT on May 7 as a positive flux patch in negative background (panel (a1)), and then the preceding polarity, "p," continuously grew in front of f (panels (a2)–(a4)). The usual spreading action drove obvious flux cancellation between the growing f and the ambient negative flux, and eventually a small filament, "F," formed between the canceling opposite-polarity magnetic fields along the eastern boundary of the AR. F started to erupt at about 19:20 UT on May 11, accompanied by an M1.1 flare with start, peak, and end times around 19:22, 19:38, and 19:55 UT, respectively. Before the eruption, F can be clearly
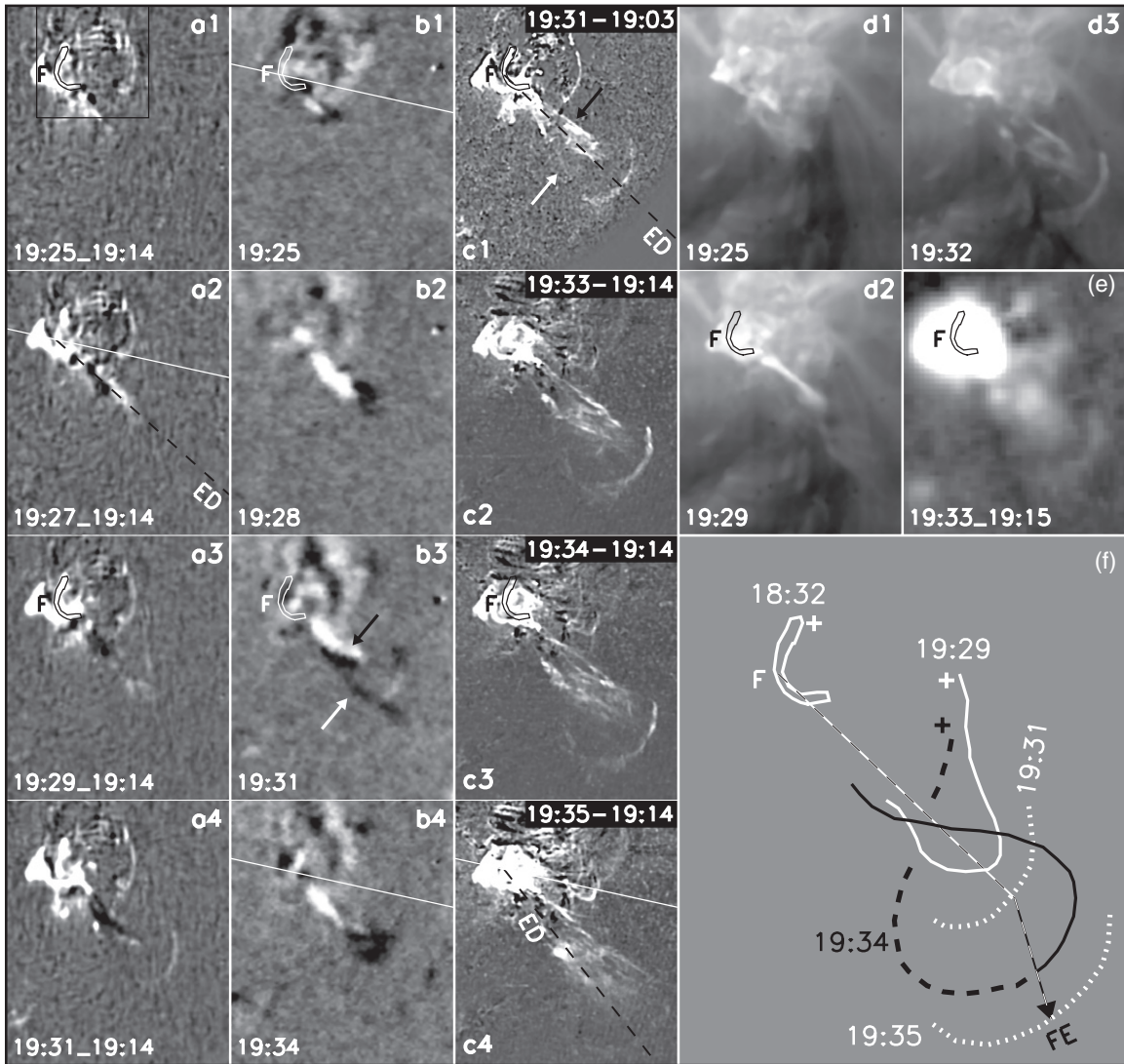
Figure 2. F eruption in BBSO Hα (a1–a4), *TRACE* 1600 Å (c1) and 171 Å (c2–c4), and SXI SXR (e) fixed-base difference images, in MLSO He 10830 Å velocity (b1–b4), and EIT 195 Å direct (d1–d3) images, with the pre-eruptive F outlines as in Figure 1 superimposed as black and white contours. The solid white lines indicate F's radial direction, and the dashed black lines, "ED," indicate F's eruption direction. In (f), the outlines of the 18:32 UT pre-eruptive Hα F, the 19:29 UT Hα cusp-like axis, the inferred 19:34 UT *TRACE* 171 Å leg-crossing pattern, and F's tops from the 19:31 and 19:35 UT *TRACE* images are plotted. The bent lines with arrowhead, "FE," indicate the clockwise deflection of ED, and the plus signs mark the northern end of the erupting F. The FOV is 220″ × 260″, and the black box indicates the FOV in Figure 1.

seen in both *TRACE* 171 Å and Hα images (panels (c) and (d1)), with centroid at a position angle (P.A.) of about 258°. Because the northern end anchored to f, the axial field of F was pointed to the left when viewed from the positive-polarity side, and thus F was a sinistral filament that obeys the chirality rule of filaments in the southern hemisphere (Pevtsov et al. 2003). Accordingly, there were some right-skewed coronal loops overlying F and connecting opposite polarities on its two sides in *TRACE* 171 Å images (Martin & McAllister 1996). Therefore, we can deduce that F and its overlying arcade had positive magnetic helicity. After the eruption, the entire F became invisible. Because F did not recover in the following 2 hr after the flare ended (panel (d2)), we can conclude that it underwent a full eruption.

The detailed eruption process is shown in Figure 2, in which F's radial direction, defined as a straight line connecting its original centroid to the solar disk center, is plotted by the solid white lines. The eruption showed three striking characteristics described as follows. First, F underwent a non-radial eruption that tilted southward from its radial direction.

This can be clearly seen by comparing the radial direction with its eruption direction, "ED," determined by a straight line connecting its erupting top to the original centroid and plotted by the dashed black lines. Second, the eruption showed clear kinking structures. F first erupted as a bright streak in Hα and EIT 195 Å images (panels (a1), (a2), and (d1)), then developed a cusp-like structure (panel (a3)), and finally transformed into a writhed structure in inverted γ shape that consisted of a bright, well-defined closed-loop apex and two crossing legs (panels (a4) and (d3)). Note that the bright apex can also be identified in the 19:33 UT SXI SXR image (panel (e)). The inverse γ-shaped structure can be seen more clearly in *TRACE* images (panels (c1)–(c4)). The foreground leg was wider and brighter than the background one. It included some bright thin threads and crossed from lower left to upper right, indicating a positive sense of writhe that matched F's chirality (Rust & LaBonte 2005; Török et al. 2010). In panel (f), the outlines of F's cusp-like axis from the 19:29 UT Hα image are plotted by the solid white curve, and the 19:34 UT leg-crossing configuration from the
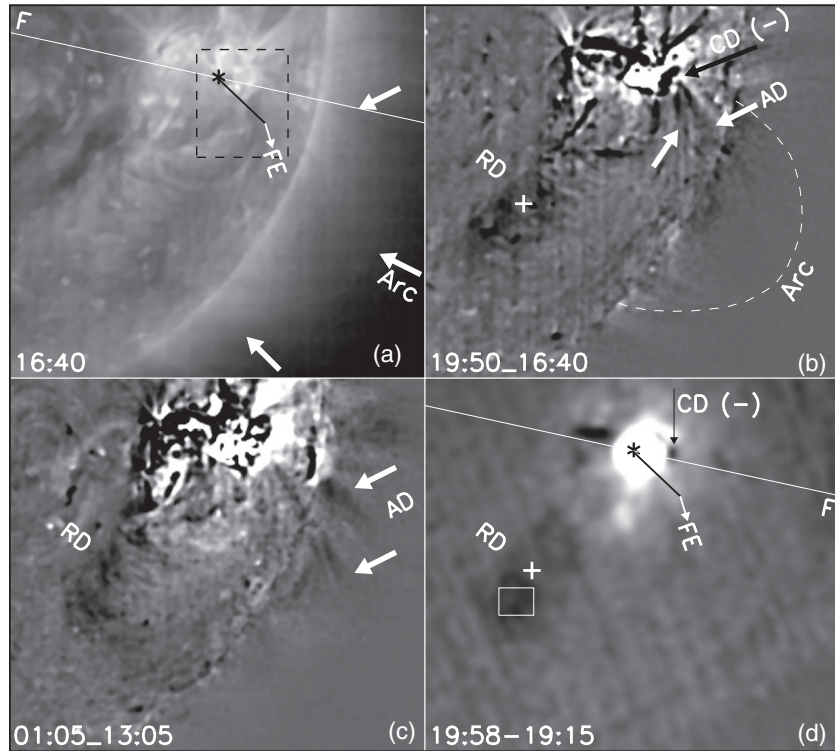
Figure 3. EIT 195 Å direct image (a) showing that the eruptive F was located in the northern flank of a coronal arcade, "Arc," indicated by the thick white arrows. EIT 195 Å (b), 284 Å (c), and SXI SXR (d) fixed-base difference images showing the associated coronal dimmings after the F eruption: a compact dimming, "CD," and leg-like dark features, "AD," close to the Arc's northern leg, as well as a diffuse remote dimming, "RD," near the Arc's southern flank. The dashed curve indicates the outermost outline of the Arc, and the plus/minus signs mark the corresponding positive/negative magnetic polarities in the photosphere. The asterisk signs mark F's original centroid, and F's radial direction and FE are also plotted. The FOV is $1000'' \times 900''$. The dotted black box indicates the FOV in Figure 2, and the solid white box marks the area in which the SXI SXR light curve is measured and displayed in Figure 5.

TRACE 171 Å image is highlighted by the black curves, with the solid/dashed lines showing the deduced front/back legs. Such a leg-crossing pattern suggests that, when seen from above, F's apex had a clockwise rotation about its eruption direction in the course of the transformation from the cusp shape into the inverse γ-shape (Green et al. 2007). The clockwise rotation was confirmed by making a comparison between the 19:31 UT *TRACE* and He I 10830 Å velocity images. It is found that the front leg was redshifted (indicated by the black arrows) while the back one was mainly blueshifted (indicated by the white arrows). Although we failed to find any rotation feature in and around F before the flare (Green et al. 2007; Liu et al. 2008; Muglach et al. 2009; Bemporad et al. 2011), it is very likely that the F eruption was driven by a kink instability of a magnetic flux rope containing F, during which the twist of the flux-rope field was converted into the writhe (Török & Kliem 2005; Fan & Gibson 2007). Because no hard X-ray observation is available for the event, however, we cannot deduce whether leg–leg reconnection occurred or not at the crossing point of the two legs (Alexander et al. 2006; Liu & Alexander 2009; Cho et al. 2009; Kliem et al. 2010). Third, ED had a clockwise deflection of about 10° from 19:31 to 19:35 UT in *TRACE* images. In panel (f), the deflection is clearly shown by the bent solid lines with arrowhead, "FE," which connected the original centroid and the apex center of the erupting F at four times. Unfortunately, there was a gap in the MLSO velocity observations from 19:37 to 19:48 UT due to bad weather conditions, and F's apex was beyond the *TRACE* FOV after 19:35 UT. The database thus does not allow us to definitely tell whether or not such a deflection is caused by an unkinking motion of the writhing F (Alexander et al. 2006; Liu et al. 2007). Another possibility is that the deflection is relevant

to the overlying coronal magnetic field. This will be discussed in the following section.

By examining the full-disk EIT 195 Å and SXI SXR observations, it is found that the F eruption was accompanied by the formation of a remote coronal dimming. Figure 3 shows the appearance of associated dimmings. Before the eruption, the EIT 195 Å direct image (panel (a)) reveals that there was a coronal arcade, "Arc," above F. As indicated by the white arrows, the original F was located in the northern flank of the Arc, but the erupting F deflected toward its central part. After the eruption, the remote dimming, "RD," clearly appeared to the southeast of the original F in the different images from the pre-event images at EIT 195 Å, 284 Å, and SXI SXR (panels (b)–(d)). The outermost outline of the Arc in panel (b) indicates that RD was located around another flank of the Arc. It was rather diffuse and about 0.4 $R_\odot$ distant from F's centroid, while a relatively compact dimming, "CD," formed adjacent to the erupted F. Compared with MDI magnetograms, RD and CD were located near the positive and negative footprint regions of the Arc, respectively. Furthermore, two leg-like dark features, "AD," appeared to connect to CD along the Arc's northern leg (indicated by the white arrows in (b) and (c)). As shown by Jiang et al. (2008) and Yang et al. (2011), therefore, it appears that RD and CD consisted of a pair of opposite-polarity dimmings as a result of the Arc's eruption forced by F's eruption, and AD just represented the disappeared loops of the Arc.

The following full halo CME first appeared in the FOV of the LASCO C2 at 20:13 UT, and later in the LASCO C3 at 20:40 UT as diffuse bright extensions above the SW limb, with a central P.A. of 233°. Figure 4 shows the associated pre-eruption coronal configuration and the appearance of the CME. The final
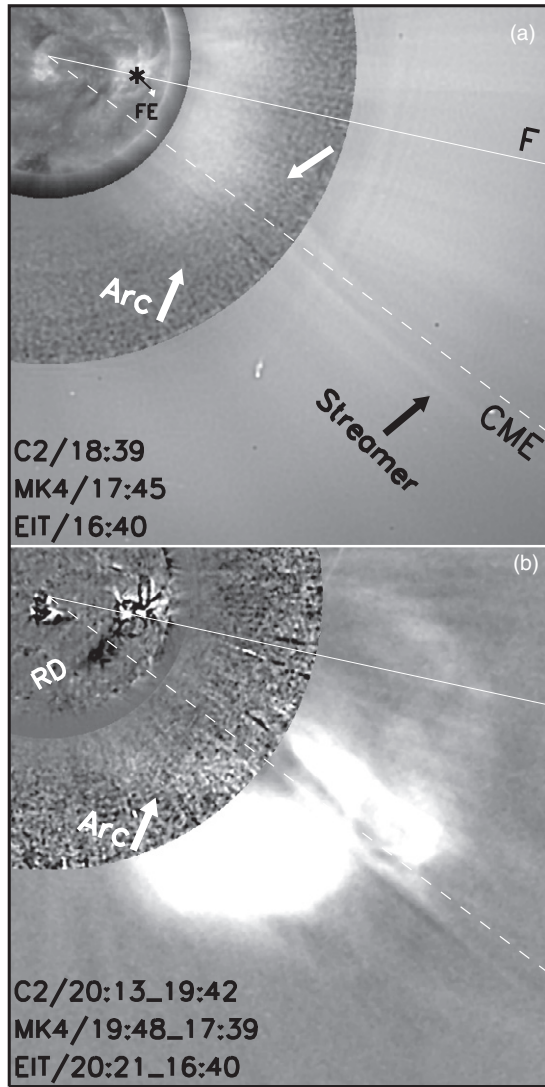
Figure 4. Combined EIT 195 Å, MLSO MK4, and LASCO C2 direct (a) and difference (b) images showing the pre-eruptive helmet streamer and the appearance of the CME. The white arrows in (a) indicate the streamer arcade, identified with Arc in the EIT direct image in Figure 3. The dashed lines indicate the final eruption direction of the CME, and F's original centroid, the radial direction, and FE as in Figure 3 are also plotted.

Figure 5. (a) F heights along the eruption direction as a function of time. The second-order polynomial fitting is given. (b) Time profile of *GOES-10* 1–8 Å SXR flux, and the light curve of SXI SXR intensities in an area centered on RD (indicated by the solid white box in Figure 3). The light curve is computed from the intensity integrated and normalized over the area. (c) Heights of the CME fronts as a function of time, and the back extrapolations by the use of second-order polynomial fitting. The vertical dashed lines indicate the start time of the flare, the vertical solid lines indicate the extrapolated onset time of the CME, the thin horizontal bar indicates the duration of the flare main phase, and the thick horizontal bars indicate the overall flare duration. The arrows indicate the approximate time of the transformation from the cusp shape into the inverse γ-shape in the erupting F.

CME direction determined from its central P.A. is plotted by the dashed white lines, F's radial direction is plotted by the solid white lines, and FE is also indicated. Consistent with the pre-eruptive EIT observation, a bright arcade-like feature, the white-light counterpart of the EUV Arc's extension, can be discerned in the MK4 FOV (indicated by the white arrows in panel (a)) before the CME, and a clear ray-like coronal streamer appeared nearly along the CME eruption direction in the C2 FOV (indicated by the black arrow). Clearly, the original F was in the northern outskirts of the streamer base, the final CME direction had a 25° lateral deflection from F's radial direction, and the clockwise deflection of the non-radially erupting F made it tend to approach the CME direction. Therefore, the halo CME can be classified as an over-and-out one according to the definition of Moore & Sterling (2007). It is noted that the Arc indeed showed an eruptive signature (indicated by the white arrow in panel (b)) underneath the CME front just before its appearanc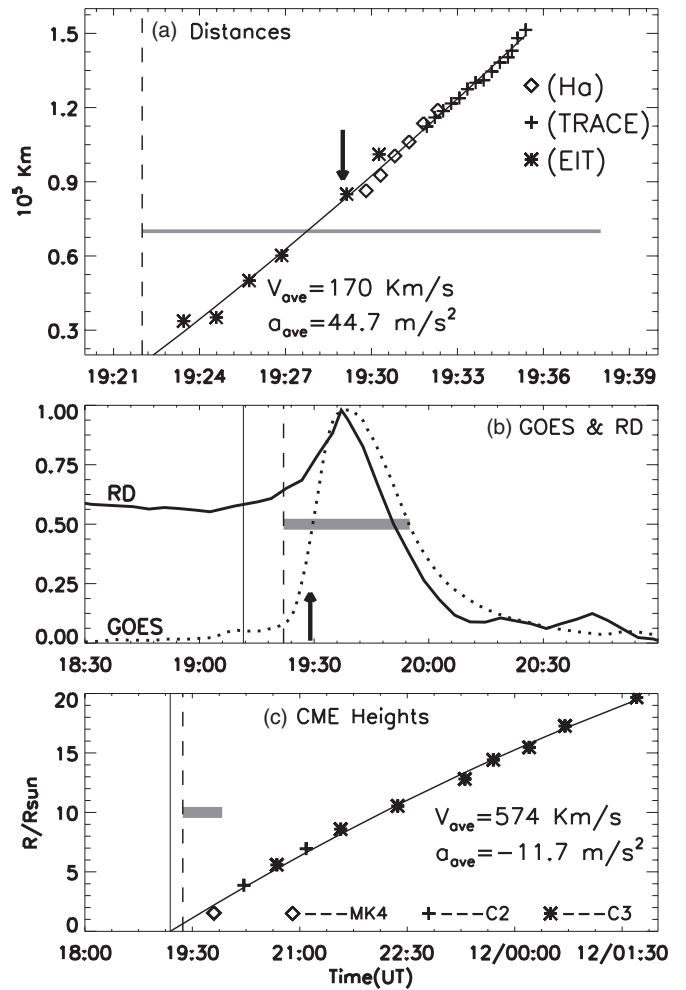e in the C2 FOV, RD was located along the CME direction, and F's rotation occurred at much lower height than that of the CME.

In Figure 5, the projected F height measured from the original centroid to the erupting top along its eruption direction on the basis of Hα, EIT, and *TRACE* observations and the light curve of SXI SXR intensities in RD are plotted and compared with the *GOES-10* 1–8 Å SXR flux and the CME front height–time (H–T) measurements. As indicated by the arrows, the erupting F rotated at the early rise phase of the flare. By using first-/second-order polynomial fitting to the measured F heights and the H–T points of the CME front, the average speed/acceleration was $170 \, \mathrm{km \, s^{-1}}/44.7 \, \mathrm{m \, s^{-2}}$ for the F eruption at the flare main phase from 19:23 to 19:35 UT, and it was $574 \, \mathrm{km \, s^{-1}}/-11.7 \, \mathrm{m \, s^{-2}}$ for the CME. These parameters indicate that F possibly underwent larger acceleration than that of the final CME (Zhang et al. 2001). Meanwhile, back extrapolation of the CME front from the H–T plots to the eruptive location by applying second-order polynomial fitting yields an estimate of the CME onset time near
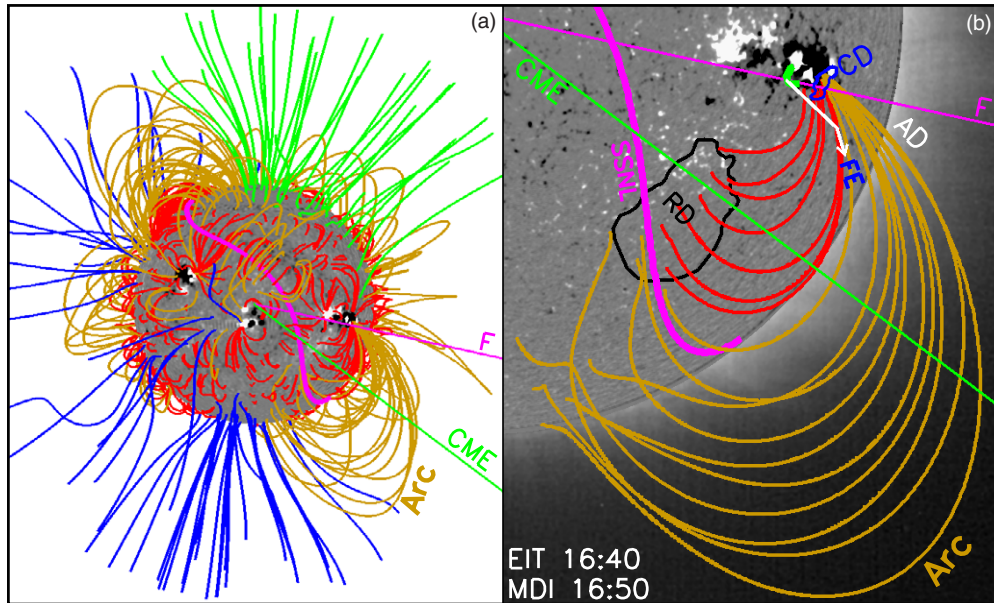
Figure 6. (a) The overall coronal field line configuration showing the helmet streamer belt. (b) Overlay of zoomed-in composite image of pre-eruptive MDI magnetogram and EIT 195 Å image with the extrapolated field lines. Open field lines directed inward and outward are coded in green and blue, respectively. Closed field lines are coded in yellow if they extend beyond 1.2 $R_\odot$, red otherwise. The pink curves are the SSNL's projection. F's radial direction (pink), FE (white), and the CME direction (green) are plotted. The outlines of the original F, RD, and CD are superimposed as green, black, and blue contours, respectively, and AD is indicated. Arc is anchored around RD and CD. The FOV for (b) is $1130'' \times 1370''$.

19:11 UT, which was close to the flare start time at 19:22 UT. An H–T point of the CME front from the MK4 image at 19:48 UT (see panel (b) in Figure 4) is also close to the extrapolated curves. Thus, the F eruption was in tight association with the CME. Because there is no full-disk EIT observation between 16:41 and 19:49 UT, the continuous SXI observations are used to measure the SXR intensities in RD. We see that at first RD intensities increased and reached maximum nearly simultaneously with the *GOES* flare peak, but then decreased obviously. Consistent with the previous observations (Toma et al. 2005; Jiang et al. 2006, 2007b), therefore, the RD formation might involve preceding brightenings that first appeared at the RD site during the flare's rise phase.

4. DISCUSSION AND INTERPRETATION

Our observations did not allow us to definitively say that the pre-eruption field containing F's material must have a flux rope configuration, but the appearance of kinking structures at the lower corona indicates that the F eruption was probably driven by the kink instability. Regarding F and its overlying loops (see Figure 1) as a flux-rope system, this means that the twist within the flux rope might reach the instability threshold before eruption onset. The twist buildup in the flux rope might be due to the flux cancellation forced by the emerging AR at the site of the F formation (van Ballegooijen & Martens 1989). As a signature of steady magnetic reconnection in the lower solar atmosphere (Wang & Shi 1993; Linker et al. 2001; Jiang et al. 2007a), the flux cancellation might also lead to tether-cutting reconnection below F and thus play a role in unleashing F by weakening its photospheric anchorage (Moore & Roumeliotis 1992). Therefore, it is probable that the triggering of the F eruption involved a combination of the kink instability and the tether-cutting reconnection (Moore & Sterling 2006; Liu et al. 2008). Because a large degree of kinking generally appears in a failed eruption instead of a full eruption (Gilbert et al. 2007), however, a natural question is raised: Why can the full

F eruption display the clear kinking structures? According to previous results (Török & Kliem 2005; Williams et al. 2005; Fan & Gibson 2007; Liu 2008), the surrounding magnetic field and its possible interaction with the erupting flux rope should be important factors in fully releasing the kink-unstable F, and further in determining the dimming configuration and the eruption deflection. To investigate such a possibility, the global coronal magnetic field configuration was computed by applying the PFSS software package available in SolarSoftWare, which is based on the PFSS model of the Schrijver & DeRosa (2003) version and synoptic magnetic maps from MDI with a 6 hr time cadence. We used the synoptic map at the time closest to the event studied here, and the result is presented in Figure 6, along with superposed outlines of the original F (green), RD (black), and CD (blue), F's radial direction (pink), FE (white), and the CME direction (green).

In line with the observations shown in Figures 3 and 4, the event was associated with the PFSS modeled bipolar helmet streamer belt (Zhao & Webb 2003) that separates opposite-polarity open field regions represented by blue and green field lines in panel (a). Yellow and red field lines in panel (b) indicate the closed bipolar field regions of the streamer close to the eruptive F, i.e., the streamer arcade that is coincident with the Arc seen in EIT EUV and coronagraph white-light images above the SW limb. The computed source surface neutral line (SSNL) defines the base of the heliospheric current sheet (HCS) (Smith 2001) at 2.5 $R_\odot$, where the radial field is set to zero. Its projection onto the photospheric magnetogram, plotted as the pink curves, is passed through the Arc. F lies in the Arc's northern flank and thus is significantly away from SSNL's projection and not along the main neutral line (NL) of the Arc. RD and CD are located in the opposite-polarity footprint regions of the Arc, while AD is coincident with the Arc's northern leg. Corresponding to the diffuse RD and the compact CD, the photospheric magnetic field settings underneath the Arc show an asymmetrical distribution that the negative-polarity footprint region is much more confined than the positive-polarity one. Obviously, the Arc's northern leg
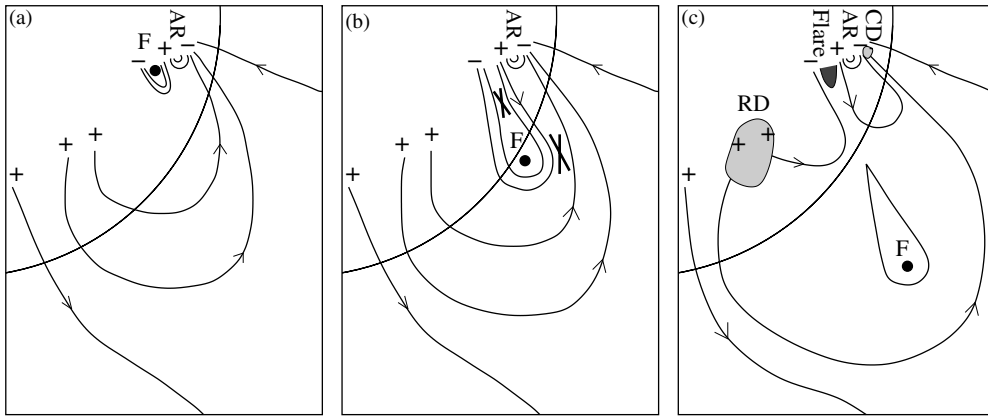
Figure 7. Sketch illustrating the non-radial F eruption and the over-and-out CME under the magnetic-arch-blowout scenario. The plus/minus signs mark the photospheric positive/negative polarities, the solid circles represent the erupting F, the elongated crosses label the internal and external reconnections, and the dark and gray patches mark the flare and dimmings, respectively. North is up and west to the right.

anchored on a small area adjacent to F, while the direction deflection of the non-radial F eruption is almost along the field lines of this leg. As described by the magnetic-arch-blowout scenario for over-and-out CMEs (Moore & Sterling 2007), therefore, it is very likely that the leg field is strong enough to laterally guide the erupting F from moving radially outward. Apart from guiding action, we speculate that such a strong leg field can also confine the flux rope and thus favor the buildup of sufficient internal twist in it for the development of the kink instability (Fan & Gibson 2007). Then, at the initial eruption phase it can suppress the flux rope, so that the kinking structures are thoroughly exposed (Gilbert et al. 2007; Kumar et al. 2011).

Based on the observations and combined with the PFSS extrapolation, the sketch presented in Figure 7 summarizes our interpretation of the event under the magnetic-arch-blowout scenario, in which only a few representative field lines are drawn and the erupting F is simply indicated by the solid circles. The initial configuration, at the stage that F is already in its critical state to erupt, is deduced from the photospheric magnetic field settings at the streamer base, and in particular, the result of the PFSS extrapolation (panel (a)). Similar to the large-scale magnetic field topology in the events studied by Bemporad et al. (2005), Li et al. (2008), and Jiang et al. (2009), such a configuration shows a quadrupolar magnetic nature, in which the presence of a null point and therefore a local field strength minimum above or near F ought to make it easier for the flux ropes to expand (Jacobs et al. 2009). It has a "negative–positive–negative–positive" photospheric polarity distribution from north to south in the streamer base and thus covers three NLs. The emerging bipolar AR forms the northernmost NL. Its following polarity (positive) cancels with negative flux to the southeast and leads to the formation of F, indicative of another NL. F is held by small overlying coronal loops (see Figure 1), and they consist of the eruptive flux rope. Next to F's south, the main NL of the streamer is concentric with the overarching streamer arcade represented by the two high field lines. At the early eruption phase, the flux rope is channeled by the streamer arcade, rises non-radially, and undergoes clockwise rotation and deflection along its northern leg. Then the further eruption leads to internal reconnection in the interior of the expanding loops, as well as external reconnection with the nearby opposite-polarity streamer arcade (panel (b)). It is noteworthy that the external reconnection is very similar to the breakout-like quadrupolar reconnection (Antiochos et al. 1999) in the full eruption of

a kink-unstable filament studied by Williams et al. (2005). It weakens the streamer arcade's tethers and might just be the release mechanism for the full F eruption. The outcome of the reconnections is shown in panel (c). The internal reconnection produces the flare in the lower atmosphere. Together with the external reconnection, the central part of the flux rope disconnects from the photosphere to generate an escaping "flux-rope plasmoid." When the plasmoid is up the leg to be near the Arc's top where the field is weaker than in the leg, it explodes radially outward and forces the stretch and expansion of an outer segment of the streamer arcade to produce the CME and the coronal dimmings at the opposite-polarity footprints. In this process, moreover, the external reconnection also produces new magnetic connections from the negative-polarity side of F to the RD region, which might be responsible for the preceding brightenings in RD.

In summary, by taking the kink instability as the driver and tether-cutting/weakening reconnections below/above F as the release mechanism, many aspects of the event can be explained well by the magnetic-arch-blowout model, in which the guiding action imposed by the northern leg of the streamer arcade is a crucial factor in producing the non-radial eruption and its deflection. Our observations also support the idea that the global background magnetic fields might control the dynamic behavior of filament eruptions and CMEs in the inner corona and further reflect the configuration of associated coronal dimmings (Démoulin 2008; Evans et al. 2011; Yang et al. 2012). First, consistent with the previous observations that the axis of CME tends to locally align itself with the HCS (Mulligan et al. 2001; Yurchyshyn 2008), the F eruption approached SSNL's projection (see Figure 6). Second, according to the results of Liu (2007) (see their Figure 4), the CME source was under the PFSS computed HCS and thus the CME had a relatively low average speed of 574 km s^{-1}. Third, the external reconnection in our explanation is supportive of the numerical simulation results that reconnection plays a significant role in rotating and deflecting a CME flux rope (Cohen et al. 2010; Shiota et al. 2010; Lugaz et al. 2011). Finally, we would like to point out that there is an alternative mechanism for the rotation of a line-tied flux rope due to the presence of an external shear field component (Isenberg & Forbes 2007). Lynch et al. (2009) argued from the breakout CME simulations that once the flare reconnection starts, almost all of the CME models are qualitatively similar and the sheared-arcade breakout eruptions can also show the same rotation and/or axial writhe previously thought to be exclusively

YANG ET AL.

signatures of pre-eruption flux-rope CME models. However, more recently Kliem et al. (2012) suggested that the contributions by shear and twist to the total rotation can be disentangled in the analysis of the eruption and rotation dynamics and in comparison to model calculations, and the resulting twist estimate allows one to judge whether the helical kink instability occurred (Thompson et al. 2012). Clearly, more observations and theoretical work are needed to detail the question further.

REFERENCES

Alexander, D., Liu, R., & Gilbert, H. R. 2006, ApJ, 653, 719
Antiochos, S. K., DeVore, C. R., & Klimchuk, J. A. 1999, ApJ, 510, 485
Bemporad, A., Mierla, M., & Tripathi, D. 2011, A&A, 531, A147
Bemporad, A., Sterling, A. C., Moore, R. L., & Poletto, G. 2005, ApJ, 635, L189
Bi, Y., Jiang, Y., Yang, L., & Zheng, R. 2011, New Astron., 16, 276
Brueckner, G. E., Howard, R. A., Koomen, M. J., et al. 1995, Sol. Phys., 162, 357
Byrne, J. P., Maloney, S. A., McAteer, R. T. J., Refojo, J. M., & Gallagher, P. T. 2010, Nat. Commun., 1, 74
Cho, K.-S., Lee, J., Bong, S.-C., et al. 2009, ApJ, 703, 1
Cohen, O., Attrill, G. D. R., Schwadron, N. A., et al. 2010, J. Geophys. Res., 115, A10104
Cremades, H., & Bothmer, V. 2004, A&A, 422, 307
Delaboudinière, J.-P., Artzner, G. E., Brunaud, J., et al. 1995, Sol. Phys., 162, 291
Démoulin, P. 2008, Ann. Geophys., 26, 3113
Evans, R. M., Opher, M., & Gombosi, T. I. 2011, ApJ, 728, 41
Fan, Y. 2005, ApJ, 630, 543
Fan, Y., & Gibson, S. E. 2007, ApJ, 668, 1232
Filippov, B. P., & Gopalswamy, N. 2001, Sol. Phys., 203, 119
Gibson, S. E., & Fan, Y. 2006, ApJ, 637, 65
Gibson, S. E., & Fan, Y. 2008, J. Geophys. Res., 113, A09103
Gilbert, H. R., Alexander, D., & Liu, R. 2007, Sol. Phys., 245, 287
Gopalswamy, N., & Thompson, B. J. 2000, J. Atmos. Sol.-Terr. Phys., 62, 1457
Green, L. M., Kliem, B., Török, T., van Driel-Gesztelyi, L., & Attrill, G. D. R. 2007, Sol. Phys., 246, 365
Gui, B., Shen, C., Wang, Y., et al. 2011, Sol. Phys., 271, 111
Handy, B. N., Acton, L. W., Kankelborg, C. C., et al. 1999, Sol. Phys., 187, 229
Harrison, R. A. 1986, A&A, 162, 283
Hill, S. M., Pizzo, V. J., Balch, C. C., et al. 2005, Sol. Phys., 226, 255
Isenberg, P. A., & Forbes, T. G. 2007, ApJ, 670, 1453
Jacobs, C., Roussev, I. I., Lugaz, N., & Poedts, S. 2009, ApJ, 695, L171
Ji, H., Wang, H., Schmahl, E. J., Moon, Y.-J., & Jiang, Y. 2003, ApJ, 595, L135
Jiang, Y., Li, L., & Yang, L. 2006, Chin. J. Astron. Astrophys., 6, 345
Jiang, Y., Shen, Y., Bi, Y., Yang, J., & Wang, J. 2008, ApJ, 677, 699
Jiang, Y., Shen, Y., & Wang, J. 2007a, Chin. J. Astron. Astrophys., 7, 129
Jiang, Y., Yang, J., Zheng, R., Bi, Y., & Yang, X. 2009, ApJ, 693, 1851
Jiang, Y., Yang, L., Li, K., & Ren, D. 2007b, ApJ, 662, L131

Karlický, M., & Kliem, B. 2010, Sol. Phys., 266, 71
Kliem, B., Linton, M. G., Török, T., & Karlický, M. 2010, Sol. Phys., 266, 91
Kliem, B., Török, T., & Thompson, W. T. 2012, Sol. Phys., submitted (arXiv:1112.3389)
Kumar, P., Srivastava, A. K., Filipov, B., Erdélyi, R., & Uddin, W. 2011, Sol. Phys., 272, 301
Li, Y., Lynch, B. J., Stenborg, G., et al. 2008, ApJ, 681, L37
Linker, J. A., Lionello, R., Mikić, Z., & Amari, T. 2001, J. Geophys. Res., 106, 25165
Liu, R., & Alexander, D. 2009, ApJ, 697, 999
Liu, R., Alexander, D., & Gilbert, H. R. 2007, ApJ, 661, 1260
Liu, R., Gilbert, H. R., Alexander, D., & Su, Y. 2008, ApJ, 680, 1508
Liu, Y. 2007, ApJ, 654, L171
Liu, Y. 2008, ApJ, 679, L151
Lugaz, N., Downs, D., Shibata, K., et al. 2011, ApJ, 738, 127
Lynch, B. J., Antiochos, S. K., Li, Y., Luhmann, J. G., & DeVore, C. R. 2009, ApJ, 697, 1918
MacQueen, R. M., Blankner, J. G., Elmore, D. F., Lecinski, A. R., & White, O. R. 1998, Sol. Phys., 182, 97
Martin, S. F., & McAllister, A. H. 1996, in IAU Colloq. 153, Magnetodynamic Phenomena in the Solar Atmosphere: Prototypes of Stellar Magnetic Activity, ed. Y. Uchida, H. Hudson, & T. Kosugi (Dordrecht: Kluwer), 497
Moore, R. L., & Roumeliotis, G. 1992, in IAU Colloq. 133, Eruptive Solar Flares, ed. Z. Švestka, B. V. Jackson, & M. E. Machado (Berlin: Springer), 69
Moore, R. L., & Sterling, A. C. 2006, in Solar Eruptions and Energetic Particles (Geophysical Monograph Series), vol. 165, ed. N. Gopalswamy, R. Mewaldt, & J. Torsti (Washington, DC: AGU), 43
Moore, R. L., & Sterling, A. C. 2007, ApJ, 661, 543
Muglach, K., Wang, Y.-M., & Kliem, B. 2009, ApJ, 703, 976
Mulligan, T., Russell, C. T., Elliott, D., Gosling, J. T., & Luhmann, J. G. 2001, Geophys. Res. Lett., 28, 891
Pevtsov, A. A., Balasubramaniam, K. S., & Rogers, J. W. 2003, ApJ, 595, 500
Romano, P., Contarino, L., & Zuccarello, E. 2003, Sol. Phys., 214, 313
Rust, D. M., & LaBonte, B. J. 2005, ApJ, 622, L69
Sakurai, T. 1976, PASJ, 28, 177
Scherrer, P. H., Bogart, R. S., Bush, R. I., et al. 1995, Sol. Phys., 162, 129
Schrijver, C. J., & DeRosa, M. L. 2003, Sol. Phys., 212, 165
Shen, C., Wang, Y., Gui, B., Ye, P., & Wang, S. 2011, Sol. Phys., 269, 389
Shiota, D., Kusano, K., Miyoshi, T., & Shibata, K. 2010, ApJ, 718, 1305
Smith, E. J. 2001, J. Geophys. Res., 106, 15819
Srivastava, A. K., Zaqarashvili, T. V., Kumar, P., & Khodachenko, M. L. 2010, ApJ, 715, 292
Sterling, A. C., Moore, R., & Harra, L. K. 2011, ApJ, 743, 63
Thompson, B. J., Plunkett, S. P., Gurman, J. B., et al. 1998, Geophys. Res. Lett., 25, 2465
Thompson, W. T., Kliem, B., & Török, T. 2012, Sol. Phys., 276, 241
Toma, G. De., Holzer, T. E., Burkepile, J. T., & Gilbert, H. R. 2005, ApJ, 621, 1109
Török, T., Berger, M. A., & Kliem, B. 2010, A&A, 516, A49
Török, T., & Kliem, B. 2005, ApJ, 630, L97
van Ballegooijen, A. A., & Martens, P. C. H. 1989, ApJ, 343, 971
Wang, J., & Shi, Z. 1993, Sol. Phys., 143, 119
Wang, Y., Shen, C., Gui, B., et al. 2011, J. Geophys. Res., 116, A04104
Webb, D. F., Lepping, R. P., Burlaga, L. F., et al. 2000, J. Geophys. Res., 105, 27251
Williams, D. R., Török, T., Démoulin, P., van Driel-Gesztelyi, L., & Kliem, B. 2005, ApJ, 628, L163
Yang, J., Jiang, Y., Zheng, R., et al. 2011, Sol. Phys., 170, 551
Yang, J., Jiang, Y., Zheng, R., et al. 2012, ApJ, 745, 9
Yurchyshyn, V. 2008, ApJ, 675, L49
Zhang, J., Dere, K. P., Howard, R. A., Kundu, M. R., & White, S. M. 2001, ApJ, 559, 452
Zhao, X. P., & Webb, D. F. 2003, J. Geophys. Res., 108, 1234
Zhou, G. P., Wang, J. X., Zhang, J., et al. 2006, ApJ, 651, 1238
Zuccarello, F. P., Bemporad, A., Jacobs, C., et al. 2012, ApJ, 744, 66